Astron. Astrophys. 350, 765–776 (1999)

ASTRONOMY AND ASTROPHYSICS

ISOPHOT observations of narrow line Seyfert 1 galaxies

M. Polletta[1,2] **and T.J.-L. Courvoisier**[1,2]

[1] Geneva Observatory, Ch. des Maillettes 11, 1290 Sauverny, Switzerland
[2] Integral Science Data Centre, Ch. d'Ecogia 16, 1290 Versoix, Switzerland

Received 31 March 1999 / Accepted 6 September 1999

Abstract. Broad infrared spectra (7–200 μm) of four NLSy1 galaxies, obtained with the imaging photo-polarimeter (ISOPHOT) on-board ISO, are presented. ISOPHOT data have been analyzed applying a (non standard) method that is described in details.

The infrared spectra of the four selected NLSy1 galaxies have been analyzed in order to derive the distribution of luminosities, temperatures, opacities and sizes of the emitting dust. A comparison between infrared ($\alpha_{3,60}$) and optical emission line (H_α/H_β and [OIII]/H_β) properties suggests that NLSy1 galaxies suffer different degrees of dust absorption according to the inclination of the line of sight.

Key words: galaxies: individual: – galaxies: photometry – galaxies: Seyfert – infrared: galaxies

1. Introduction

Narrow-line Seyfert 1 galaxies (NLSy1) are defined by their optical emission line properties: permitted lines are only slightly broader than the forbidden lines, and narrower than in typical Seyfert 1 galaxies (FWHM (H_β) $\simeq$ 500–2000 km s^{-1}); strong emission features from FeII (optical multiplets centered at 4750, 5190 and 5300 Å), and high-ionization optical lines are often present (Osterbrock & Pogge 1985; Goodrich 1989), and forbidden lines emission is relatively weak ([OIII]/$H_\beta < 3$). Although the emission lines widths and ratios have given a designation to this class long ago, it is only recently that the singular nature of these objects has been discovered thanks to X-ray observations. Indeed, many NLSy1 have soft X-ray spectra much steeper than in normal broad emission lines Seyfert 1 galaxies (photon index $\Gamma \simeq$ 3–5), and the soft X-ray emission shows rapid and/or large amplitude variations (Boller et al. 1996). In spite of the different spectral shape, the soft X-ray luminosities are similar to those observed in Seyfert 1 galaxies. At higher energies ($>$ 2 keV) the NLSy1 galaxies show a relatively weak hard power law, slightly steeper than observed in Seyfert 1 galaxies (Brandt et al. 1997; Otani et al. 1996; Comastri et al. 1998; Pounds et al. 1995). Several NLSy1s have exceptionally strong EUV/soft X-ray excesses, when normalized by the optical/UV continuum (Rodríguez-Pascual et al. 1997). A red optical continuum spectrum and relatively strong infrared (IR) emission are observed in several NLSy1s (Halpern & Oke 1987). In the far-IR (FIR) and radio domains the NLSy1s show a high degree of similarity with normal Seyfert 1 galaxies (Rodríguez-Pascual et al. 1997; Ulvestad et al. 1995).

The relative weakness of low density forbidden line emission and the absence of broad hydrogen wings in NLSy1 galaxies may be understood if most of the ionizing flux is absorbed in the inner forbidden line region, thus reducing the amount of ionizing radiation reaching the low density clouds, and absorbing the internal broad-line region. Absorbing dust in the circumnuclear environment is then a likely cause for the peculiar emission line properties in NLSy1 galaxies. This hypothesis has also been suggested by spectropolarimetry and soft X-ray observations. Spectropolarimetry observations indicate that dust scatters the optical photons in several NLSy1 galaxies (Goodrich 1989), and soft X-ray observations indicate the presence of a dusty warm absorber along the line of sight of some NLSy1 galaxies (Komossa & Greiner 1998).

Our purpose is to investigate the role of the dust in NLSy1 galaxies through the analysis of their infrared (IR) emission. The IR radiation in Seyfert galaxies can be considered as the direct tracer of dust (Barvainis 1990; Clavel et al. 1989). The infrared emission carries information on dust at different scales, and temperatures: on cool dust (T = 15–35 K) in the interstellar medium heated by the stellar radiation field of the host galaxy at 1.5 kpc, on warm starburst-related dust (T = 20–50 K) at few hundred, and/or kiloparsec scales, and on AGN-related dust extending from 1 pc to 1 kpc (T = 35–2000 K). A well sampled infrared spectral energy distribution is necessary to trace the dust distribution from the circumnuclear region to the kiloparsec scales of the host galaxy.

The Infrared Space Observatory (ISO; Kessler et al. 1996) has devoted several programs to study NLSy1 galaxies observing in total 16 NLSy1s at several wavelengths between 7 and 200 μm. Results obtained with the Imaging Photo-Polarimeter (ISOPHOT; Lemke et al. 1996) on board ISO for four NLSy1 galaxies (TONS180, RXJ0323-49, IRAS13224-3809, and PG1404+226) are presented here. We also present observations at millimeter and near-infrared wavelengths of the

Send offprint requests to: Maria.Polletta@obs.unige.ch

selected NLSy1 galaxies that have been performed to complete, and better sample their infrared spectral energy distribution (SED).

2. Observational dataset

We selected four NLSy1 galaxies on the basis of their singular behaviour in the ultraviolet and/or soft X-ray energy bands (see classification and optical spectra in Grupe 1996, Boller et al. 1993, Véron-Cetty & Véron 1998). Source names, coordinates and redshifts, taken from the Nasa Extragalactic Database (NED)[1], are listed in Table 1. In order to study their infrared emission we performed a program of observations that has involved several observatories: the Infrared Space Observatory, the IRAM interferometer on Plateau de Bure in France (Guilloteau et al. 1992), the IRAC1 and the Swedish ESO Submm Telescope (SEST) telescopes of the European Southern Observatory (ESO) at La Silla.

ISOPHOT observations have been performed for all the selected sources, while just few objects have been observed with the other observatories listed above. ISOPHOT observations and data reduction are described in the next section.

TON S180, and IRAS 13224-3809 have been observed in the near-IR with the IRAC1 telescope on June 21^{st}, 1996. We measured a flux density of 23 ± 2 mJy in the L($3.7\,\mu$m) photometric band, and of 29 ± 9 mJy in the M($4.7\,\mu$m) photometric band from TON S180, and of 11 ± 1 mJy in the L photometric band from IRAS 13224-3809. IRAS 13224-3809 has also been observed at millimeter wavelengths with the SEST telescope on November 3^{th}, 1995. The measured flux density is 21 ± 10 mJy at 1.3 mm after reduction to outside the atmosphere, correction for the gain elevation characteristic of the telescope, and calibration with Uranus. The NLSy1 PG 1404+226 has also been observed at millimeter wavelengths, using the IRAM interferometer on Plateau de Bure on May 19^{th}, 1998. Three of the five antennas in compact configuration have been used, and 3C 273 was the calibrator. PG1404+226 was observed during 2.6 hours. We measured a flux density of 1.97 ± 1.55 mJy at 112.0 GHz, and 10.03 ± 7.2 mJy at 230.5 GHz. All the millimeter data show a very low signal to noise ratio, therefore we allot 3σ upper limits to the fluxes.

3. ISOPHOT observations and data reduction

Photometric data at 9 wavelengths between 7.3 and 200 μm have been obtained for each object using the P1, P2, C100, and C200 detectors. The P1, and P2 detectors have been used for the short wavelength observations. They are single detectors collecting a fraction of the source signal depending on the chosen aperture. The observations have been performed through a circular aperture of $13.8''$ in diameter at 7.3 μm, of $23''$ at 12 μm, and of $52''$ at 25 μm in order to have the same intensity fraction (90%) of the source flux at each wavelength. For long wavelength observations the C100 and C200 array cameras have been used. They have respectively nine, and four detector pixels each covering respectively an area of $43.5'' \times 43.5''$, and $89.4'' \times 89.4''$ on the sky. All the observations have been performed deflecting the radiation beam from the source (on-source position) to adjacent fields on the sky (off-source position) several times in order to measure the background emission (chopper observing mode). Triangular and rectangular chopping modes have been used. In the triangular chopper mode the background emission is measured in two different regions, while in the rectangular chopper mode it is measured in only one position. Observing dates, filters, exposure times, chopping mode, and measured fluxes are reported in Table 2.

[1] The NASA/IPAC Extragalactic Database (NED) is operated by the Jet Propulsion Laboratory, California Institute of Technology, under contract with the National Aeronautics and Space Administration.

Table 1. Basic properties

Source Name	RA (2000) ($h\ m\ s$)	Dec (2000) ($^\circ\ '\ ''$)	z
TON S180	00 57 19.9	−22 22 59	0.062
RX J0323.2-4931	03 23 17.2	−49 30 50	0.071
IRAS13224-3809	13 25 19.6	−38 24 55	0.067
PG 1404+226	14 06 21.9	+22 23 47	0.098

3.1. First steps of the data reduction: from ERD to AAP level

The first part of the data reduction has been performed using version 7.3 of the ISOPHOT Interactive Analysis (PIA) tool (Gabriel et al. 1997). We used the raw data that have been processed with version 7.0 of the Off-Line Processing (Laureijs et al. 1998). The raw data form a sequence of detector readouts distributed in 2^n (n is an integer between 2 and 6) sets of four response curves or ramps, according to the integration time (Edited Raw Data: ERD in Volts). Each set of four ramps represents a chopper position (on- and off-source). Each ramp is corrected for the non-linearity of the detector response, and for contamination of cosmic particle events (glitches). Two criteria are applied to recognize and remove read-outs affected by glitches. Those read-outs at more than 4.5σ from the average are removed. Among the remaining values, the read-outs at more than 3.0σ from the new average and the subsequent data points are removed until the value has decreased to 1σ from the average (see the PIA User manual for more details; Gabriel et al. 1998). After applying the non-linearity correction, and the deglitching to the ERD, a straight line is fitted to each ramp, in order to determine its slope or Signal per Ramp Data (SRD in Volt/s).

The SRD are corrected for highly discrepant points (value at more than 3σ from the average signal) still contaminated by glitches, for the orbital dependent dark current, and for the signal dependence on the ramp integration time (reset time interval) to obtain an average Signal per Chopper Plateau (SCP in Volt/s).

After applying flat-fielding correction, the SCP data are calibrated to obtain the Standard Processed Data (SPD in unit of Watts). Since the detector response varies with time, it is determined at the time of the observation by measuring the flux

emitted by two thermal Fine Calibration Sources (FCS1 and FCS2) on board. Data from FCS1 are used because they are the best calibrated. The FCS1 signal is checked in order to remove data with large uncertainties. The removal of data with large uncertainties is equivalent to using the weighted mean of all FCS1 data. After the flux calibration the AAP (Auto Analysis Product) data are obtained. They are a sequence of 2^n off- and on-source flux measurements (in Jansky) each corresponding to a chopper position. The reduction from the AAP level to the final results is performed using our own IDL routines, and not following the standard pipeline.

3.2. From the AAP level to final results

The last steps of the data reduction before determining the source flux, are the background subtraction, the deletion of remaining highly discrepant points, and the correction for transient effects, vignetting and point spread function.

In the case of the C100 detector only the central pixel pointed on the source is considered to derive the flux density since the eight border pixels contain only a small fraction of the central point source and summing these values would therefore only increase the noise (but see Sect. 4). In the case of the C200 detector the source signal is equally distributed on the four pixels of the array, therefore the final source flux is computed by adding the values measured by each pixel.

3.2.1. Background subtraction

The background is measured at each off-source position. Since in some cases the instruments show long term drift effects (the measured signal varies with observation time), the background signal is re-estimated in order to remove this effect. New background estimations are obtained by computing the weighted mean of each couple of consecutive off-source measurements. These computed background fluxes are then subtracted from the on-source values measured in between each couple of off-source measurements. In Fig. 1 the data obtained from RXJ0323-49 with the central pixel of the C100 detector at 80 μm are reported to illustrate the method. In this example the data are two series of eight on-source ($\diamond$), and eight off-source ($\times$) measurements. The computed background values (B) are represented by squares ($\square$) (the meaning of empty and filled symbols is described in the following section). Since the sequence of chopper plateau ends with an on-source position, we used the weighted mean of the two last on-source measurements, and the flux observed in the last off-source position to have the last couple of on- and off-source values. After subtraction of the background estimates (B) from the associated on-source measurements (S), 2^{n-1} source flux measurements are obtained. These values are further checked before computing the final source flux.

3.2.2. Deletion of remaining highly discrepant points

At this reduction level a further check of the data is required, since instability effects of the detectors may still affect the data.

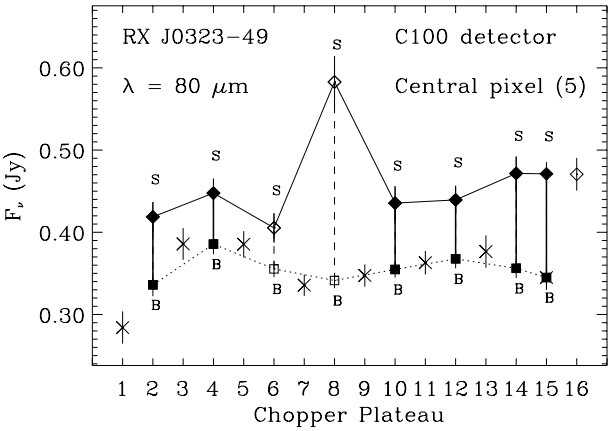

Fig. 1. AAP data of the central pixel (5) of the C100 detector obtained for the observation of RXJ0323-49 at 80 μm. $\diamond$ represent on-source measurements, $\times$ off-source measurements, $\square$ interpolated off-source measurements. The last on-source value is obtained by interpolating two on-source measurements. Selected couples of off- and on-source measurements after deletion of discrepant points are indicated by filled symbols (see Sect. 3.2.2).

Such effects are not yet well known, it is therefore difficult to recognize and remove them. We resort to a simple method based on statistics, and not on the *a priori* knowledge of most recurrent observed effects. With the assumption that the differences between each couple of on- (S) and off-source (B) values are normally distributed around the weighted mean value with a width given by the measured standard deviation of the distribution, all the measurements with values that are less probable than a limit defined on the basis of the number of available points can be rejected (Chauvenet's criterion in Taylor 1982). An example of the application of this criterion is shown in Fig. 1. Among the eight differences obtained from all the couples of on- (S) and off- (B) values, the Chauvenet's criterion selects six couples S-B (thick solid lines) indicated by filled symbols, and rejects two couples S-B (dashed lines). The final source flux is derived from the weighted mean of all the selected differences S-B. The associated uncertainty is the standard deviation of the weighted mean σ_S. If the measured fluxes are smaller than σ_S, an upper limit to the flux is given equal to 5σ, where σ is the standard deviation of the whole distribution of differences.

In the C100 observation at 80 μm of TON S180 the Chauvenet's criterion rejects the only two flux values available because they are at more than $1.15\sigma_S$ from the weighted mean. However, since our criterion takes into account only statistical uncertainties and not systematic errors, that are of the order of 30% (see Sect. 3.3), and since the two measurements are consistent at 2.5σ with the weighted mean, we consider the final flux value as reliable.

3.2.3. Vignetting correction

C100 and C200 data are further corrected for the signal loss outside the beam of the telescope (vignetting). The PIA default vignetting correction factors have been computed considering the

dependency only on the distance of the chopper positions and on the filter, but recent investigations have shown that they depend also on the time per chopper plateau (M. Haas, private communication). The PIA vignetting correction factors may overestimate the flux value. In order to estimate the effects of this correction, we compared the results obtained without correcting for vignetting with the corrected fluxes. The median value of the computed differences expressed in percentage is 2% for the C100 data, and 67% for the C200. The vignetting correction for the C100 data is negligible, therefore we adopted the fluxes corrected for vignetting using the PIA default values. On the contrary, in the case of the C200, the vignetting correction is very large. Since the right correction factors are not yet available, new estimations for the C200 data are obtained averaging the vignetting corrected, and the not corrected values. Since the values corrected for vignetting and those not corrected have different statistical uncertainties, the uncertainty σ_{tot} we use is the quadratic sum of the uncertainties σ_i obtained in the two cases. If both the measured fluxes are smaller than their own uncertainties σ_i, an upper limit to the flux is given equal to $5\sigma_{tot}$. If at least one measurement is larger than its uncertainty σ_i, but the average flux is smaller than σ_{tot}, an upper limit to the flux is given equal to the maximum flux value (the maximum flux value is the corrected for vignetting flux) plus the corresponding σ_i.

3.2.4. Correction for transient effects and point spread function

A correction for the signal loss due to transient effects depending on the time per chopper plateau is applied to the computed fluxes. Since short integration times do not permit to the C100, and C200 detectors to reach the full signal, the observed flux can be reduced by large factors, typically up to 68% for the C100 detector, and up to 12% for the C200 detector for the shortest observations. The correction factors we use are the PIA default values.

The computed fluxes are finally corrected for the point spread function (psf) of each detector by using the default PIA values derived empirically. In the case of the C200 detector the theoretical point spread function values are slightly different from the empirical values (Laureijs et al. 1998), and the difference becomes important ($\sim$30%) at 200 μm. We used different point spread function correction factors for vignetting corrected fluxes, and not corrected ones, in order to have the largest difference between the two values. For P1, P2, and C100 data we use the PIA default psf values.

3.3. Calculation of systematic uncertainties

During the data reduction only statistical errors have been taken into account, however the accuracy of the absolute photometric calibration depends mainly on systematic errors (detector transient effects, calibration response, dark current, point spread function), and it is currently known to be better than 30% (Klaas et al. 1998). Therefore we associate to the measured flux an uncertainty that is the quadratic sum of their σ_S and the 30% (for the C200 measurements we use 67% to take into account the uncertainty in the vignetting correction) of the measured value. The associated statistical and systematic uncertainties are reported in the last two columns of Table 2. These values will be used in the following fitting procedure of the spectral energy distributions (SEDs).

Table 2. Details of ISOPHOT Observations

Det.	λ (μm)	Exp. (s)	Chopper Mode	F_ν (mJy)	Uncertainty† Stat.	Syst.
TON S180 (Obs. date: June 06, 1997)						
P1	7.3	128	T	33.7	1.5	10.
P1	12	64	T	113.	3.	34.
P2	25	128	T	159.	30.	48.
C100	60	128	R	412.	25.	124.
C100	80	16	R	406.	54.	122.
C100	100	128	R	235.	16.	71.
C200	150	128	R	184.	22.	123.
C200	170	128	R	179.	22.	120.
C200	200	128	R	$<$216.		
RX J0323.2-4931 (Obs. date: June 16, 1997)						
P1	7.3	512	T	5.0	1.8	1.5
P1	12	256	T	20.9	3.2	6.3
P2	25	512	T	26.5	7.9	8.0
C100	60	128	R	243.	31.	73.
C100	80	128	R	246.	24.	74.
C100	100	128	R	270.	33.	81.
C200	150	128	R	270.	41.	181.
C200	170	128	R	187.	34.	125.
C200	200	128	R	$<$300.		
IRAS 13224-3809 (Obs. date: August 23, 1996)						
C100‡	60	64	R	1346.	194.	404.
C100‡	80	64	R	3208.	170.	962.
C100‡	100	64	R	2744.	171.	823.
C200	150	64	R	1357.	52.	909.
C200	170	64	R	1451.	50.	972.
C200	200	64	R	833.	150.	558.
PG 1404+226 (Obs. date: December 22, 1996)						
P1	7.3	2048	T	6.3	0.5	1.9
P1	12	1024	T	18.4	4.9	5.5
P2	25	2048	T	$<$91.41		
C100	60	128	R	84.	20.	25.
C100	80	128	R	144.	29.	43.
C100	100	128	R	160.	18.	48.
C200	150	128	R	389.	36.	261.
C200	170	128	R	269.	25.	180.
C200	200	128	R	175.	50.	117.

† In units of mJy. ‡ Obtained considering all the pixel of the detector array.

4. Comparison with IRAS

All four NLSy1s have been previously observed by IRAS. The fluxes in the four IRAS bands have been taken from the NED database. All the objects have been detected previously by IRAS

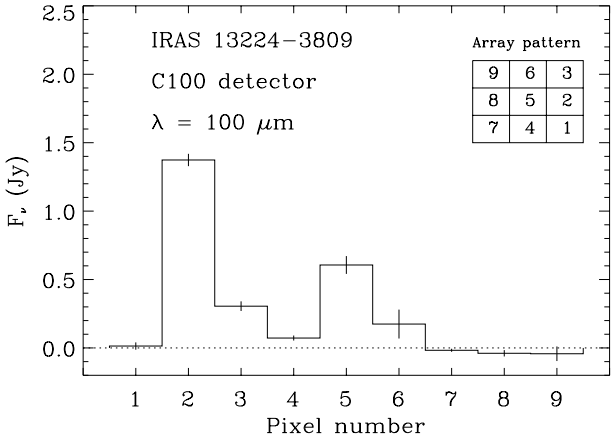

Fig. 2. Measured source flux by each pixel of the C100 detector of IRAS 13224-3809 at 100 μm. Dotted line represents the zero level flux.

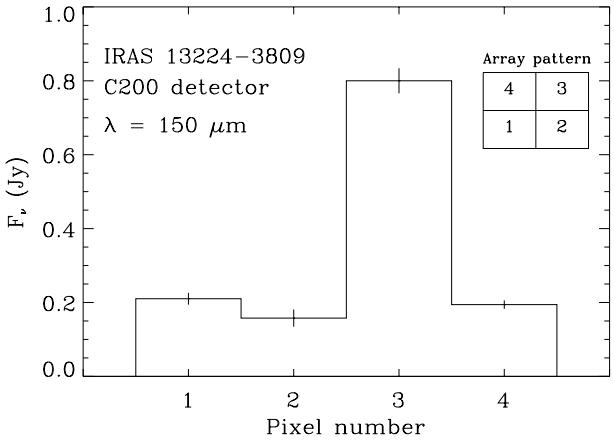

Fig. 3. Measured source flux by each pixel of the C200 detector of IRAS 13224-3809 at 150 μm.

in at least two filters, with the exception of PG1404+226 for which IRAS has given only upper limits. ISOPHOT gives in most cases results consistent with IRAS data (within 1σ, and within 2.2σ at 25 μm for RXJ0323-49), and supplies new measurements to IRAS upper limits. However, large differences are obtained for IRAS 13224-3809. At long wavelengths both IRAS and ISO detected IRAS 13224-3809, but consistent values (within 1σ) are obtained only if all the pixels of the C100 detector are taken into account. The fluxes measured by the central pixel are indeed 44% and 39% of the fluxes obtained by using all pixels, respectively at 60 and 100 μm. Looking at the signal obtained by each pixel of the C100 camera an excess in between pixel 2 is observed at all three filters, as shown in Fig. 2 for λ=100 μm. Moreover, an excess in pixel 3 is measured by each filter of the C200 detector, as shown in Fig. 3, where the vignetting corrected C200 data at 150 μm are shown.

A check of the pointing of the instruments has revealed an incorrect reference position for the source, that is located outside the beam of the P1, and P2 detectors, between pixel 2, and 5 of the C100 detector, and in pixel 3 of the C200. The position of each pixel projected on the sky, and the source position are

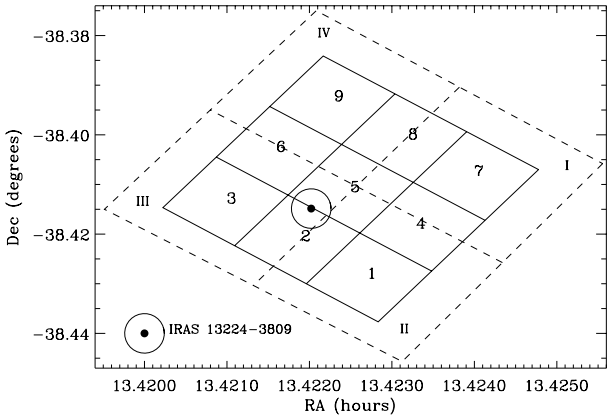

Fig. 4. Projection of the C100 (solid line), and C200 (dashed line) detectors on the sky region covered during the observation fo IRAS 13224-3809. The circle indicates the position of the source on the sky (NED). The number 1-9 indicate the pixels of the C100 detector, and I-IV the pixels of the C200. The coordinates are at epoch 2000.

shown in Fig. 4. The cause of the bad pointing was the use of wrong source coordinates. Unfortunately we cannot use P1, and P2 data, since the source was outside the instruments beams, but the long wavelength measurements can be used provided that we take data from all the pixels. With this choice also the data of IRAS 13224-3809 are consistent with IRAS results at 60, and 100 μm.

5. Spectral fits

All the data for the four objects considered in this study have been converted to monochromatic luminosities in the rest frame of the object (H_0 = 75 km s^{-1} kpc^{-1}) using the following equation:

$$L_{\nu em} = 4\pi d_L^2 F_{\nu obs}/(1+z)\,, \tag{1}$$

where $F_{\nu obs}$ is the monochromatic flux in the observer's frame, and d_L is the luminosity distance to the object:

$$d_L = \frac{cz(1+z/2)}{H_0(1+z)}\,, \tag{2}$$

The SEDs of each object are shown in 5, 6, 7, and 8.

Assuming that the infrared emission in NLSy1 galaxies is thermal as observed in normal Seyfert 1 galaxies, the grey body radiation model can be used to fit the observed SEDs. An isothermal grey body at the temperature T emits at the frequency ν a flux density given by the following equation (Gear 1988):

$$F_\nu = \Omega \cdot B(\nu, T) \cdot (1 - e^{-\tau}) \tag{3}$$

where Ω is the solid angle subtended by the source, $B(\nu, T)$ is the Planck function for a blackbody of temperature T, and τ is the optical depth of the dust. We derived the optical depth from the extinction curve computed by Draine & Lee (1984) for a mixture of graphite and silicate grains with radii varying between 0.005 and 0.25 μm (Mathis et al. 1977). The derived optical depth curve is reported in Fig. 9 for an hydrogen column

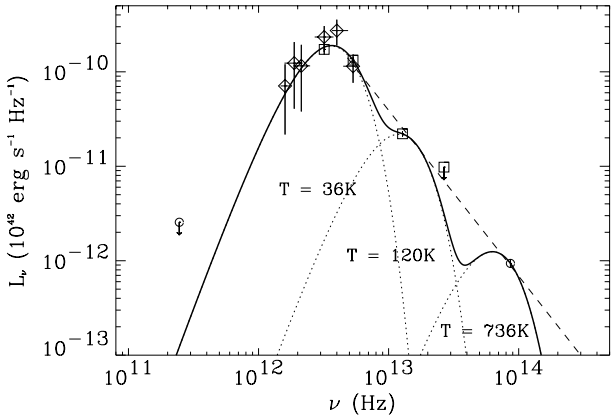

Fig. 5. Spectral energy distribution of IRAS 13224-3809 considering data from all the pixels of the C100 and of the C200 detectors. Dotted lines represent single grey body components at the indicated temperature, and the solid line the composite spectrum obtained summing each single component. The dashed line represents the power law obtained fitting data between 3 and 60 μm. Arrows indicate 5σ upper limits (3σ for millimeter data). Diamonds are ISOPHOT data, squares are IRAS data, circles are IRAC1, and SEST data.

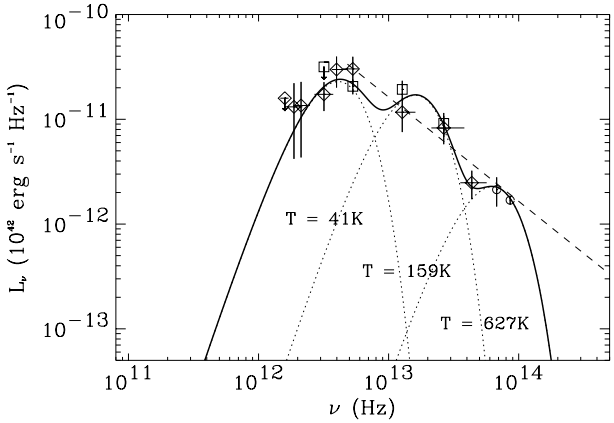

Fig. 6. Spectral energy distributions of TONS180. The symbols and the curves have the same meaning as in Fig. 5.

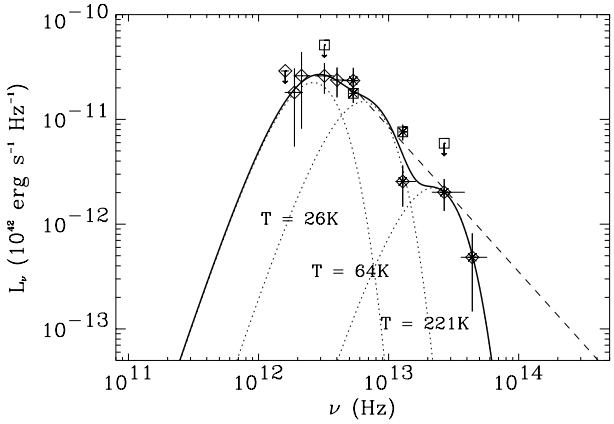

Fig. 7. Spectral energy distribution of RXJ0323-49. The symbols and the curves have the same meaning as in Fig. 5.

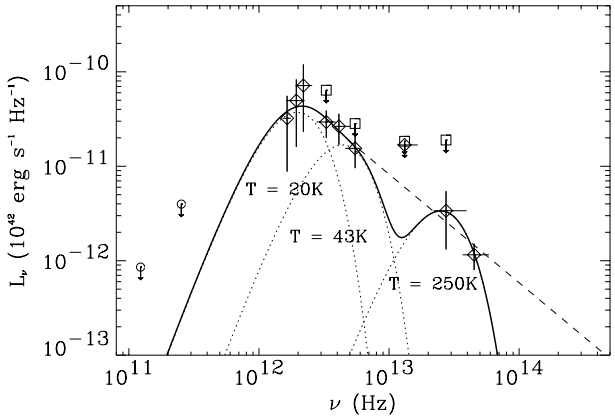

Fig. 8. Spectral energy distribution of PG 1404+226. The symbols and the curves have the same meaning as in Fig. 5. IRAM data are reported with circles.

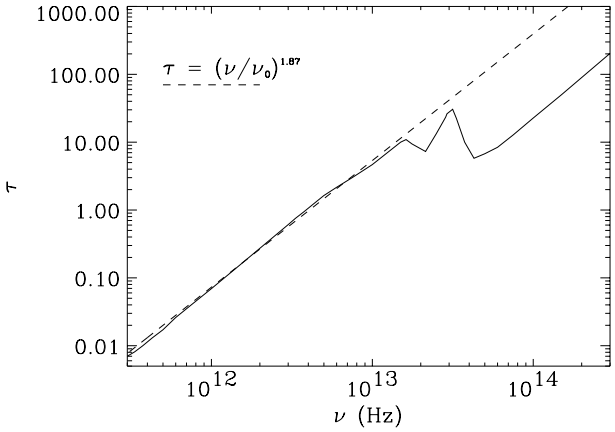

Fig. 9. Optical depth curve derived for a mixture of graphite and silicate grains (Draine & Lee 1984) scaled to a hydrogen column density of $1.\cdot10^{24}$ cm^{-2}. The dashed line represents the power law approximation of the optical depth in the wavelength range 20–500 μm adopted in this paper.

density of 10^{24} cm^{-2}. The optical depth dependence on the frequency can be approximated by a power law of type $\tau = (\nu/\nu_0)^{\beta}$, where β expresses the dependence of the dust emissivity on the frequency ($\propto \nu^{\beta}$). The power law approximation is valid only in some wavelength ranges: 1–7 μm, and 20–500 μm, because of the silicate feature at 10 μm. A power law with β equal to 1.87 is a good fit to the optical depth curve, as shown by the dashed curve superimposed to the optical depth curve in Fig. 9. The normalization of the curve is given by ν_0 that is strictly related to the hydrogen column density. We derived the following relationship between the hydrogen column density N_H and the value of ν_0:

$$N_H = C \cdot \nu_0^{-\beta} \qquad \text{atoms cm}^{-2} \tag{4}$$

where ν_0 is expressed in Hz, and C = $3.85\cdot10^{47}$, in the requested unit, in the wavelength range 20–500 μm, and C = $6.33\cdot10^{48}$ in the wavelength range 1–7 μm. Note that this relationship gives the same extinction cross section (τ/N_H) as that measured at 250 μm by FIRAS and DIRBE for dust at high galactic lati-

tude (Boulanger et al. 1996). The observed infrared SEDs are smooth and indicate a wide and probably continuous range of temperatures, not describable by a single grey body component, but rather by several grey body components at different temperatures. A non-linear least squares fit was used in the fitting procedure leaving free the solid angle Ω, and the temperature T, while the frequency ν_0 (hence the hydrogen column density) and the emissivity exponent β have been fixed. We assumed β equal to 1.87. The choice of the value of ν_0 is critical, because it is strictly related to the opacity of the source, and then to its size. Indeed, the value of Ω changes dramatically when ν_0 varies. The relationship between Ω and the size of the source (R) is $\Omega = \pi R^2/d_L^2$. In order to illustrate the effect of the choice of ν_0, we considered two extreme opacity regimes to model the observed SED of IRAS 13224-3809 from 60 to 200 μm. First, we fixed ν_0 to $3.0{\cdot}10^{12}$ Hz, corresponding to a hydrogen column density of $1.8{\cdot}10^{24}$ atoms cm^{-2}, and secondly we chose the ν_0 value corresponding to a hydrogen column density of $5.3{\cdot}10^{21}$ atoms cm^{-2}. The first value corresponds to one of the highest hydrogen column density values measured in Seyfert galaxies. The second one corresponds to the optical extinction estimated from the Balmer decrement observed in IRAS 13224-3809 (Boller et al. 1993). It has been derived using the relationship between the Balmer decrement and the optical extinction, valid for photo-ionized zones (case B) (Ward et al. 1987):

$$A_V = 6.67 \cdot log\left(\frac{\mathrm{H}_\alpha/\mathrm{H}_\beta}{2.85}\right) \quad (5)$$

and assuming the canonical relations: N_H = $5.8{\cdot}10^{21}$ E(B-V) cm^{-2} mag^{-1}, and A(V)/E(B-V) = 3.1 (Whittet 1992). The temperature, and the size of the source obtained fitting the SED of IRAS13224-3809 in the two different regimes of opacity are illustrated in Fig. 10 and in Fig. 11, where the line contours in the size and temperature plane are shown. In the case of lower opacity (ν_0 higher, and N_H lower) the source region is more extended and the equilibrium temperature of dust grains is lower than in the case of higher opacity ($\sim$4500 pc in size and 36 K in temperature in the low opacity case as opposed to $\sim$200 pc and 45 K in the high opacity case).

We applied both models also to the observed SEDs of the other three NLSy1 galaxies. In the high opacity model the same hydrogen column density of $1.8{\cdot}10^{24}$ cm^{-2} used for IRAS 13224-3809 has been assumed. In the low opacity case we assumed a hydrogen column density corresponding to that derived from the measured Balmer decrement value for PG1404+226, and RXJ0323-49 (respectively N_H=$1.07{\cdot}10^{21}$ cm^{-2}, and $1.97{\cdot}10^{21}$ cm^{-2}) (Miller et al. 1992, and Grupe 1996). While for TON S180 we chose the column density associated to our Galaxy in the direction of the source (N_H=$1.55{\cdot}10^{20}$ cm^{-2}, Dickey & Lockman 1990). This assumption is justified by a measured Balmer decrement value (Comastri et al. 1998) that is lower than expected in the case of no reddening.

The best fitting curves in the low opacity case of the observed infrared SEDs are shown in Figs. 5, 6, 7, and 8. The thick solid line represents the sum of the grey bodies, each one of which is shown with a dotted line. Spectra fitted with the high opacity model are not shown because their spectral shape is very similar to those given.

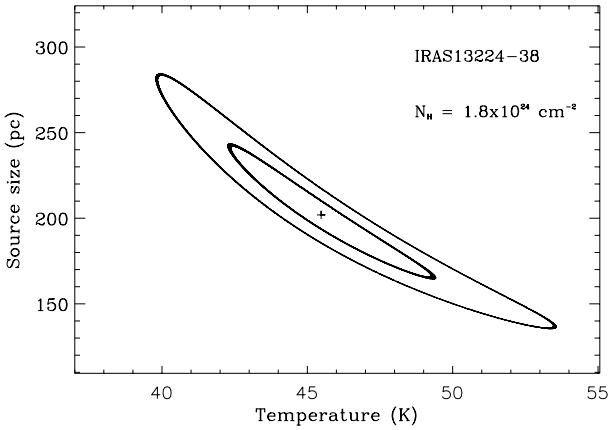

Fig. 10. Contour plot in the source size and temperature plane for the cold component of IRAS 13224-3809 in the high opacity model. Line contours are at 90%, and 99% confidence limits.

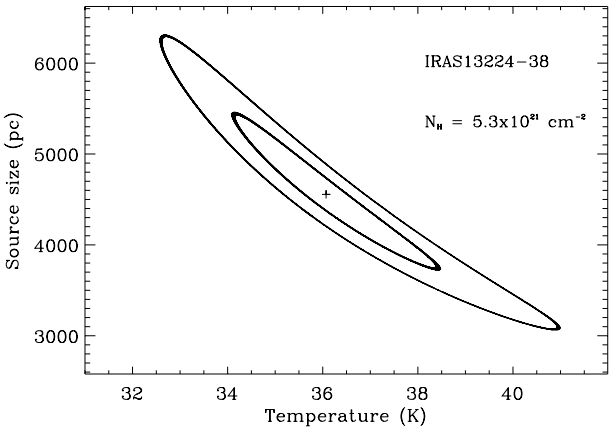

Fig. 11. As in Fig. 10, but for the low opacity model.

6. Discussion

6.1. Dust opacity

Any model which seeks to explain the entire infrared emission in terms of thermal dust emission must involve a dust distribution with a range of temperatures, opacities, and distances from the heating source. It is not realistic to expect that dust at different temperatures will have the same optical depth because density and size are likely to differ. The real opacities of the NLSy1 galaxies are probably intermediate between the two extreme solutions considered above. The data do not constrain them, neither favor one of the two extreme solutions ($\Delta\chi^2_\nu \sim$ 0.001–0.015). However, indications on dust opacity can be derived by considerations on dust distribution.

Since the two extreme regimes imply dusty region sizes that are very different, a comparison with those expected by current models for Seyfert galaxies may give indications on the more likely model.

Table 3. Best fit parameters of the infrared spectra.

Source Name	High opacity T (K)	High opacity R (pc)	Low opacity T (K)	Low opacity R (pc)
TON S180	50	56	41	6924
TON S180	229	4.2	159	215
TON S180	1002	0.2	627	2.8
RX J0323-49	29	173	26	5648
RX J0323-49	81	21	64	527
RX J0323-49	315	1.1	221	10
IRAS 13224-38	45	202	36	4555
IRAS 13224-38	164	8.4	120	84
IRAS 13224-38	598	0.5	736	0.3
PG 1404+226	20	487	20	19977
PG 1404+226	52	51	43	1932
PG 1404+226	320	1.4	250	12

The temperatures and the sizes obtained in the two opacity cases for each grey body component are listed in in Table 3. In the case of large opacities the estimated sizes of the dust emission regions vary from 0.2 pc for the hottest component (1000 K), to $\sim$ 500 pc for the coldest one (20 K), and in the case of low opacities the minimal estimated size is 0.3 pc, and the maximal 20 kpc. In current models for Seyfert galaxies hot dust (T = 1000–2000 K) is located just outside of the broad line region ($\sim$ 0.1–1 pc from the central engine), warm dust (T = 35–250 K) in the narrow line region (10–2000 pc), and dust at several temperatures (T = 50–1000 K) in a dusty torus extending from 1 pc to 1 kpc. In some Seyfert galaxies star forming regions at few hundred parsecs, up to kiloparsec scales can also contribute to the observed IR emission by heating dust up to T = 35–50 K. The same distribution of sizes and temperatures as observed in Seyfert galaxies can be derived if the emitting dust heated by an ultraviolet source of Seyfert galaxies luminosity is characterized by low opacity. Indeed the temperature T of dust grains at a distance r from a central heating source of luminosity L_{UV} is given by (Barvainis 1987):

$$T = \left[\frac{L_{UV} e^{-\tau_{UV}}}{Q_\nu \nu^{-\beta}} \frac{c^2 h^{3+\beta}}{32\pi^2 r^2 k^{4+\beta}} \frac{1}{\Gamma(4+\beta)\zeta(4+\beta)} \right]^{\frac{1}{4+\beta}} \quad (6)$$

where Γ is the gamma function, ζ is the Riemann zeta function, τ_{UV} is the dust optical depth to the ultraviolet continuum, and Q_ν is the absorption efficiency of the dust grains equal to $Q_{ext}(V) \cdot \tau(\nu)/\tau(V)$ (Bianchi, Davies and Alton 1999), where $Q_{ext}(V)$ is respectively equal to 0.076, and 3.2976, for dust grain radii of 0.01, and 0.1 μm. (Draine 1985). Assuming β=1.87, Eq. 6 becomes:

$$T = F \cdot \left[\frac{L_{UV,44} \cdot e^{-\tau_{UV}}}{r_{pc}^2} \right]^{\frac{1}{5.87}} \qquad K \quad (7)$$

where F, expressed in the required unit, is equal to 560 for dust grain radii of 0.1 μm, and to 1064 for dust grain radii of 0.01 μm, $L_{UV,44}$ is the ultraviolet luminosity in units of 10^{44} erg s^{-1}, and r_{pc} is the distance from the central source in parsecs. If we assume that the total absorption of the primary UV radiation by the grains occurs at τ_{UV} = 3 (Barvainis 1987), the distances and the corresponding temperatures will be the same as those observed in Seyfert galaxies. The resulting range of values for UV luminosities of 10^{43} erg s^{-1} to 10^{45} erg s^{-1}, and for grain radii of 0.01 to 0.1 μm is represented in Fig. 12 by the region comprised between the two solid lines. The parameters obtained in the low, and high opacity regimes are also reported in the figure. As expected, the computed parameters assuming τ_{UV} = 3 are in good agreement with those derived in the low opacity case. The high opacity case is also acceptable, but only for the high temperature components. The comparison between the estimates of temperatures and sizes obtained in the two extreme regimes, and the observed values in Seyfert galaxies thus suggest that cold dust is characterized by low opacities, while the warm/hot dust may also be more opaque. In consequence, the IR reradiation at long wavelengths (T $\leq$ 60 K) will be isotropic, and orientation-independent. On the contrary, at shorter wavelengths (T $>$ 60 K) the dust may self-absorb its emitted radiation, and the observed emission may depend on orientation.

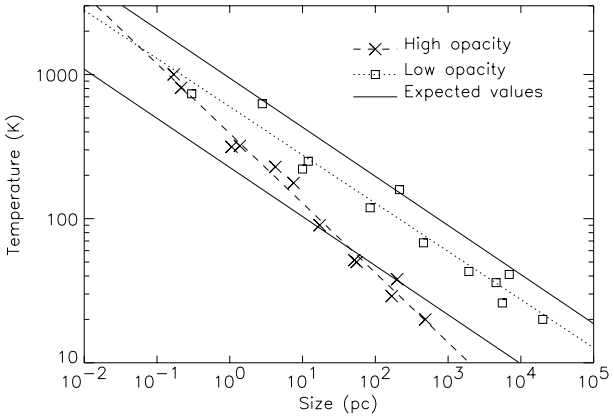

Fig. 12. Temperature and source size for each grey body component in the low opacity (□), and high opacity (×) regimes. The dotted line is the best fit linear interpolation of low opacity parameters, and the dashed line of high opacity parameters. The region within solid lines represent the parameter space for dust grain with radius = 0.01–0.1 μm, and UV optical depth τ_{UV} =3, heated by UV luminosities L_{UV} = 0.1–10·10^{44} erg s^{-1} (see Sect. 6.1).

6.2. Infrared luminosities

Previous work on the infrared emission of NLSy1 galaxies (Halpern & Oke 1987) indicate high infrared luminosities as a property of this class of objects. Although the number of objects is small to produce meaningful statistics, we tried to see if this property characterizes also the NLSy1 galaxies studied here. The infrared luminosity of our NLSy1 galaxies has been computed by integrating all the fitted grey body components in the entire observed infrared range (see Table 4), and compared with those typical of broad emission line Seyfert 1 galaxies. The most luminous objects of our sample, IRAS 13224-3809, and TON S180, belong to the category of luminous IR galaxies

Table 4. Infrared continuum properties, and optical extinction.

Source Name	L^a_{IR}	$\alpha^b_{25,60}$	$\alpha^c_{3,60}$	A^d_V
TON S180	13.8	0.3	0.99	....
RX J0323-49	6.4	1.2	1.38	1.05
IRAS 13224-38	34.5	2.0	1.77	1.84
PG 1404+226	6.5	...	1.22	0.57

[a] In unit of 10^{10} $L_\odot$. [b] Spectral index computed between 25 and 60 μm assuming $L_\nu \propto \nu^{-\alpha}$. [c] Spectral index computed between 3 and 60 μm assuming $L_\nu \propto \nu^{-\alpha}$. [d] Derived from the Balmer decrement using Eq. 5.

(L_{IR} >10^{11} $L_\odot$). The observed IR luminosities are in the same range as that of normal Seyfert galaxies.

6.3. Starburst contribution

A recurrent question in the study of the infrared emission of Seyfert galaxies is the presence of a starburst, and its contribution to the observed emission. The presence of a starburst region has been found in a similar fraction of NLSy1, and of classical Seyfert 1 galaxies by Mas-Hesse et al. (1995) by identifying the dominant heating source. Starbursts tend to generate more emission from cool dust than from hot dust when compared to AGN heated sources. The presence of this excess can therefore be recognized looking at the mid- and far-IR spectral shape. Indeed steep far/mid-IR spectra ($\alpha_{25,60}$ >1.25 where $L_\nu \propto \nu^{-\alpha}$) are typical of star forming regions, while flat far/mid-IR spectra ($\alpha_{25,60}$ = 0.50–1.25) are typical of AGNs (de Grijp et al. 1987; Mas-Hesse et al. 1994).

The far/mid-IR spectral slope has been estimated for IRAS 13224-3809, TON S180, and RXJ0323-49 because flux measurements at 25, and 60 μm are available, and not for PG 1404+226 (Table 4). TON S180, and RXJ0323-49 have $\alpha_{25,60}$ $\leq$1.2 consistent with those observed in AGN dominated Seyfert galaxies, however the contribution from a weak star forming region cannot be excluded. The steep value found for IRAS 13224-3809, instead, suggests the presence of a component of cool dust that may be heated by a starburst.

6.4. The role of the dust in NLSy1 galaxies

The presence of dust in the nuclei of Seyfert galaxies can alter the way in which we perceive these objects. Dust can absorb the optical and ultraviolet continuum (reradiating this energy in the infrared), steepen the hydrogen line decrement, and block the soft X-rays. Several estimates of the extinction due to the presence of dust along the line of sight can be derived from observations at different energies, and a comparison among them can be an indicator of the dust distribution. The extinction due to the dust along the line of sight cannot be derived from the optical depth observed in the IR, because the observed IR SEDs do not allow us to constrain it. The observed SEDs give just a range of wavelengths (from $\sim$ 1 to less than 100 μm) at which the dust could become transparent. However, it is possible to derive an estimate of the dust extinction from the observed IR SEDs by measuring the steepness of the power law obtained by fitting all the IR data at wavelengths shorter than 60 μm, where the effects of opacity become important. If the distribution of dust with radius is characterized by a constant covering factor (fraction of the sky covered by dust, as seen by the central continuum source) the emitted spectrum will have a power law shape of type $L_\nu \propto \nu^{-\alpha_{int}}$. Apparently steeper spectra may indicate that self-absorbed emission prevents short wavelength radiation from escaping (case *1*), or that the properties in the dust distribution are not the same in different objects (case *2*), i.e. the contribution from cool/cold dust is very high compared to that from the hot one.

In the first case (case *1*) steeper spectra indicate higher extinction. The extinction can be estimated if we know the intrinsic infrared spectrum, and if we can measure the emerging one. The amount of visual extinction internal to the selected sources required to steepen the power law index from α_{int} to the observed α will be:

$$A_V = \frac{(\alpha_{int} - \alpha_{\lambda_1,\lambda_2}) \cdot ln(\lambda_1/\lambda_2)}{ln\left(10^{0.4(R_{\lambda_1} - R_{\lambda_2})}\right)} \quad (8)$$

where λ_1 and λ_2 are the (rest) wavelengths between which the spectral index is measured and the function R(λ) = $\frac{A_\lambda}{A_V}$ is the reddening law at the wavelength λ (Clavel 1998). The extinction in magnitude A_λ is proportional to the optical depth $\tau(\lambda)$, thus the function R(λ) can be derived from the extinction curve. If we take as extinction curve that from which we have derived the optical depth curve reported in Fig. 9 (Draine & Lee 1984), and, if we choose λ_1 = 3 μm, and λ_2 = 60 μm, Eq. 8 becomes:

$$A_V = 77.44 \cdot (\alpha_{3,60} - \alpha_{int}) \quad (9)$$

If all the emitting warm/hot dust is also responsible for the reddening of the Balmer lines, the optical extinction as derived in Eq. 9 will be the same as that obtained using Eq. 5. This assumption leads to the following relationship between the spectral slope $\alpha_{3,60}$ and the Balmer decrement:

$$\alpha_{3,60} = 0.086 \cdot log(H_\alpha/H_\beta) + \alpha_{int} - 0.039 \quad (10)$$

In order to test this prediction we compared the H_α/H_β values of the NLSy1 galaxies studied here with the slope of the power law obtained by fitting the observed data between 3 and 60 μm. This wavelength range has been chosen in order to have the best IR slope estimate. A broad wavelength range will contain more data. We did not extended further the wavelength range because at $\lambda > 60$ μm a power law is on many cases not a good description of the spectrum, and at $\lambda < 3$ μm the flux may arise from another source, and thus turn over showing a near-IR excess. The infrared data have been fitted with a weighted least-square method. The weights have been computed assuming symmetrical uncertainties given by the half of the difference between the logarithm of the measured value plus its uncertainty and the measured value minus its uncertainty. This last hypothesis allows us to apply the χ^2 test to test the fit. The χ^2 test shows that a power law fit is acceptable at more than 99.86% of confidence. The best fit IR power laws are shown by the dashed lines

in Figs. 5, 6, 7, and 8. The best-fit slope values are reported in Table 4. The flattest slope is $\alpha_{3,60}$ = 0.99 for TONS 180, and the steepest one is $\alpha_{3,60}$ = 1.77 for IRAS 13224-3809. The measured power law slopes vary in a range of 0.78, that corresponds to a range in the visual extinction values of 61 mag, provided that all objects have the same α_{int}. The variations in the H_α/H_β values correspond, instead, to a range in the visual extinction values of only 2.84 mag. Such a difference indicates that all the emitting dust can not be responsible for the reddening observed in the Balmer lines. In other words, the $\alpha_{3,60}$ values vary with the H_α/H_β ratios more rapidly than predicted in Eq. 10.

Interestingly, this comparison has permitted to discover a strong correlation between the two parameters: H_α/H_β, and $\alpha_{3,60}$ for the selected sources. The correspondent values and their linear interpolation are shown in Fig. 13, respectively with filled diamonds, and a dashed line. The linear correlation coefficient is 0.99, and the probability to obtain such a value from not correlated values is 0.80% (significance of the correlation at a 2.66 sigma level). A stronger correlation is indicated by the non-parametric Spearman's test for which the coefficient rank is 1.0, with a null associated probability to obtain such a value from not correlated values.

Since our sample contains very few sources, a research in the literature has been performed in order to extend it and check whether this correlation is a general property of NLSy1 galaxies. We selected 12 additional NLSy1 galaxies (Mrk957, IZw1, Mrk359, IRAS02262-4110, MRK142, MRK734, NGC4051, PG1211+143, Mrk766, MRK684, MRK478, and Mrk493) among a sample of 148 objects, classified as NLSy1 in the literature[2]. The following selection criteria have been applied: 1) availability of, at least, one Balmer decrement measurement (45 objects remain); 2) availability of, at least, three flux measurements at 3 different wavelengths between 3 and 60 μm (18 objects remain); 3) the largest difference between two Balmer decrement measurements, for the same source, had to be smaller than 2 (16 objects remain); and finally 4) the infrared spectrum had to be well described by a power law in the 3–60 μm wavelength range (12 objects remain). The Balmer decrement values for these sources have been taken from the literature[3]. In case of more than one measurement the median value was chosen. The infrared data have been retrieved from NED, and then fitted with a weighted least-square method, as for the initial sample of 4 NLSy1 galaxies. The observed correlation is still present with the additional 12 NLSy1 galaxies, as shown in Fig. 13 by the solid line that represents the best fit line obtained considering all the 16 NLSy1 galaxies. The additional 12 NLSy1 galaxies are reported with empty diamonds in Fig. 13. For the whole sample (16 objects) the linear correlation coefficient is 0.71, and the probability to obtain such a value from not correlated values is 0.41%, (significance at a 2.87 sigma level). For the same sample a non-parametric Spearman's test gives a correlation coefficient of 0.61, with an associated probability to obtain such a value from not correlated values of 1.13% (significance at a 2.54 sigma level).

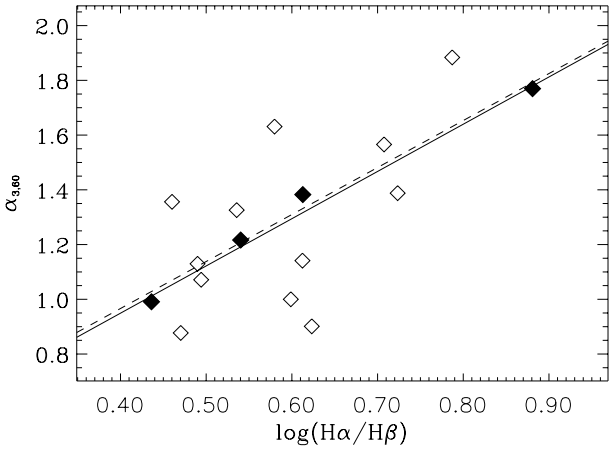

Fig. 13. Balmer decrement values vs the infrared spectral index α obtained fitting a power law in the 3–60 μm range. Filled diamonds represent the four NLSy1 galaxies of our sample, and empty diamonds twelve additional NLSy1 galaxies. The solid line is the best linear fit obtained considering all the sixteen NLSy1 galaxies, and the dashed line is the best linear fit obtained considering only the four NLSy1.

The (weak) correlation between the infrared spectral slope and the Balmer decrement could be due to a selection effect, i.e. sources with flatter IR spectra and higher Balmer decrement may be absent because of a bias in the sample due to the selection criteria or to observational effects. Such a bias is not known to us. On the other side, a real physical link between the infrared and optical properties could be hidden by the difficulties in emission lines ratio measurements.

We performed another comparison between the optical and the IR properties of this kind of objects by using the ionization parameter, given by the line intensity ratio [OIII]/H_β available for the great majority of the sources. We searched in the literature[4] for the available measurements of this ratio for all the selected sources. In few cases more than one measurement has been found, thus the median value was computed, as done for the Balmer decrement data. The result of the comparison between the infrared spectral slope $\alpha_{3,60}$, and the ionization parameter [OIII]/H_β is shown in Fig. 14: the [OIII]/H_β ratio increases when $\alpha_{3,60}$ increases. The two parameters are correlated significantly (Spearman's coefficient rank of 0.78, that is significant at 99.96%, that means at a 3.12 sigma level). If the correlations between the emission line ratios H_α/H_β and [OIII]/H_β, and the IR spectral slope $\alpha_{3,60}$ are real, a link between the processes that steepen the IR power law, and those that increase the lines ratios should be present. We have already examined the principal causes of a steepening of the IR spectrum (cases *1* and *2*

[2] Véron-Cetty M.-P., & Véron 1998; Grupe 1996; Osterbrock & Pogge 1985; Bischoff & Kollatschny 1999; Giannuzzo et al. 1998; and Wisotzki & Bade 1997.

[3] Giannuzzo et al. 1998; Osterbrock & Pogge 1985; Halpern & Oke 1987; De Zotti & Gaskell 1985; Grupe 1996; Berriman 1989; Dahari & De Robertis 1988; Halpern & Moran 1998; Mulchaey et al. 1994; Grupe et al. 1998; and Miller et al. 1992.

[4] Osterbrock & Pogge 1985; Halpern & Oke 1987; Grupe 1996; Dahari & De Robertis 1988; Grupe et al. 1998; Miller et al. 1992; Moran et al. 1996; Goodrich 1989; and Comastri et al. 1998.

above). Higher Balmer decrement values can be produced by dust reddening, and/or by radiative decay of the hydrogen atoms in which lower levels may be over-populated by collisional excitation in a dense plasma. The ionization parameter depends on the intensity of the ionizing source impinging on the NLR, and on the physical properties of the emitting gas (ionizing continuum, NLR density, and distance between the ionizing source and the emitting medium), while it does not depend strongly on the reddening from intervening material. An analysis of all the listed causes of steepening of the infrared power law, and of enhancement of the Balmer decrement, and of the ionization parameter, indicates that the observed correlations can be interpreted in terms of inclination dependent obscuration. Since the opacity of the dust responsible for the bulk of the observed IR emission is higher than that of dust attenuating the optical lines, these two dust components are distinct, but related (as indicated by the correlations of Figs. 13, and 14). This may be the case if the central regions of these objects are surrounded by a distribution of dust which becomes gradually less opaque along some directions, i.e. near to the axial direction of a dusty torus, and if the BLR is more extended than the inner hot dust (see the proposed scenario in Fig. 15). It is worth to note that the presence of line emitting gas extending further out than in normal Seyfert 1 galaxies is suggested by the observed width and variability properties of the emitted optical lines in NLSy1 galaxies (Giannuzzo et al. 1998). At low inclinations of the line of sight to the torus axis the BLR and the hottest dust component will be directly visible, while, at higher inclinations, the BLR, and the hottest dust component will be reddened since they will be observed through a dusty path. In this case the radiation coming from the extended BLR goes through dust less opaque than the hot dust radiation that is located along the torus plane. At higher inclinations of the line of sight the H_β emission coming from the BLR will decrease, while the [OIII]/H_β values associated to the NLR will be unchanged. Since we have not distinguished the H_β emission Balmer lines coming from the two regions, the observed [OIII]/H_β ratios will be enhanced at higher inclinations.

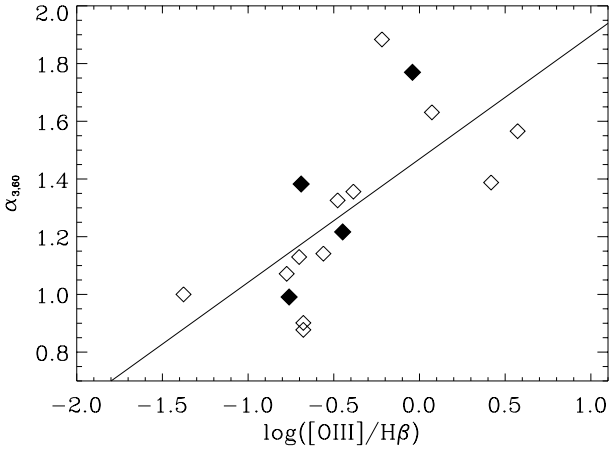

Fig. 14. Ionization indicator [OIII]/H_β versus the infrared spectral index $\alpha_{3,60}$. The solid line is the best linear fit obtained considering all the sixteen NLSy1 galaxies. Filled diamonds represent the four NLSy1 galaxies analyzed here, and empty diamonds twelve additional NLSy1 galaxies. The solid line is the best linear fit obtained considering all the sixteen NLSy1 galaxies.

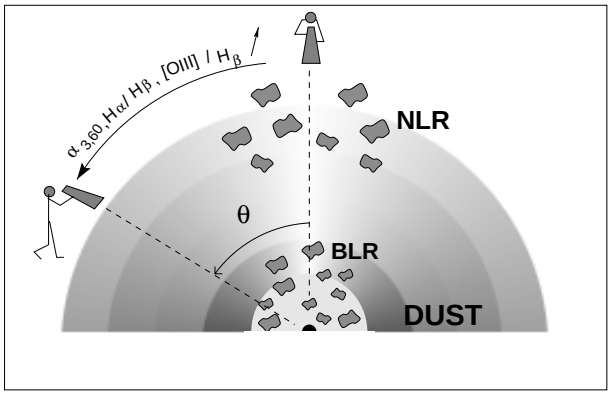

Fig. 15. Representation of the proposed scenario explaining the observed correlations. The gray rings represent the dust distribution. The dust temperature decreases at larger radii, and the opacity increases for larger values of the θ angle. Balmer lines are emitted in the BLR and in the NLR. The forbidden lines, as [OIII], are produced in the NLR by the ionizing continuum coming from the central region. The hot dust component in the inner region is partially absorbed by the dust at larger distances. At large values of the θ angle the BLR lines emission is absorbed by the dust producing higher Balmer decrements values, the host dust emission is reduced by self-absorption, and because of lower H_β emission from the BLR, and unchanged [OIII]/H_β from the NLR, the observed [OIII]/H_β ratio increases (see text for more details).

7. Conclusion

The broad band IR spectra provided by ISOPHOT for the four selected NLSy1 galaxies have allowed us to derive the distribution of temperatures of the emitting dust, and a possible range of opacities, and sizes. The comparison with current models of dust distribution in Seyfert galaxies favors lower opacities ($N_H \sim 1{\cdot}10^{21}\,cm^{-2}$) for dust at low temperatures ($T \leq 60\,K$), while warm/hot dust nearer to the heating central source may be characterized by higher opacities, and thus by an anisotropic emission.

The observed IR luminosities, and spectra are consistent with those of broad emission line Seyfert 1 galaxies. The presence of dust heated by a bright star forming region is suggested only for one of the four selected NLSy1 galaxies. It is, therefore, not a general property of NLSy1 galaxies.

A correlation between the Balmer decrement values, and the ionization parameters [OIII]/H_β with the slopes of the observed IR spectra measured for a small sample of NLSy1 galaxies (16 objects) is reported. The proposed scenario explains these correlations in terms of inclination dependent obscuration. In the case of high inclination angles, the radiation coming from an extended BLR is reddened by low opacity dust, while the hot dust radiation is absorbed by higher opacity dust located along the

torus plane. For low inclinations of the line of sight the nuclear region is directly visible and no absorption effect is observed.

This interpretation is in contradiction with the model proposed by Ulvestad et al. (1995) in which the NLSy1 galaxies are the pole-on equivalent of Seyfert 2 galaxies.

Acknowledgements. We are grateful to R. Walter, S. Paltani, and D. Carrillo for preparing the observation program. We thank the Time Allocation Committee for awarding discretionary ISO observing time to this project. Martin Haas, Péter Ábrahám, B. Wilkes, and Eric J. Hooper are acknowledged for help in the ISOPHOT data reduction. R. Neri, and D. Nuernberger are acknowledged for assistance in the IRAM interferometer data reduction. We are also very grateful to the referee, J. Clavel, for carefullly reading this manuscript and for useful comments. The ISOPHOT data presented in this paper were reduced using PIA, which is a joint development by the ESA Astrophysics Division and the ISOPHOT consortium.

References

Barvainis R., 1987, ApJ 320, 537
Barvainis R., 1990, ApJ 353, 419
Berriman G., 1989, ApJ 345, 713
Bianchi S., Davies J.I., Alton P.B., 1999, A&A 344, L1
Bischoff K., Kollatschny W., 1999, A&A 345, 49
Boller T., Trümper J. Molendi S., et al., 1993, A&A 279, 53
Boller T., Brandt W.N., Fink H., 1996, A&A 305, 53
Boulanger F., Abergel A., Bernard J.-P., et al., 1996, A&A 312, 256
Brandt W.N., Mathur S., Elvis M., 1997, MNRAS 285, L25
Clavel J., Wamsteker W., Glass I., 1989, ApJ 337, 236
Clavel J., 1998, A&A 331, 853
Comastri A., Fiore F., Guainazzi M., et al., 1998, A&A 333, 31
Dahari O., De Robertis M.M., 1988, ApJS 67, 249
de Grijp M.H.K., Lub J., Miley G.K., 1987, A&AS 70, 95
De Zotti G., Gaskell C.M., 1985, A&A 147, 1
Dickey J.M., Lockman F.J., 1990, ARA&A 28, 215
Draine B.T., Lee H.M., 1984, ApJ 285, 89
Draine B.T., 1985, ApJS 57, 587
Gabriel C., Acosta-Pulido J., Heinrichsen I., et al., 1997, "The ISOPHOT Interactive Analysis PIA, a calibration and scientific analysis tool. In: Hunt G., Payne H.E. (eds.) Proc. of the ADASS VI Conference, ASP Conf. Ser. Vol. 125
Gabriel C., Haas M., Heinrichsen I., Tai-Dias W.-M., 1998, The ISOPHOT Interactive Analysis User Manual
Gear W.K., 1988, In: Wolstencroft R.D., Burton W.B. (eds.) Millimetre and Submillimetre Astronomy
Giannuzzo M.E., Mignoli M., Stirpe G.M., Comastri A., 1998, A&A 330, 894
Goodrich R.W., 1989, ApJ 342, 224
Grupe D., 1996 Ph.D. Thesis, Göttingen Univesity
Grupe D., Wills B.J., Wills D., Beuermann K., 1998, A&A 333, 827
Guilloteau S., Delannoy J., Downes D., et al., 1992, A&A 262, 624
Halpern J.P., Oke J.B., 1987, ApJ 312, 91
Halpern J.P., Moran E.C., 1998, ApJ 494, 194
Laureijs R.J., Klass U., Richards P.J., Schulz B., 1998, ISOPHOT Data Users Manual Version 4.0, SAI/95-220/Dc
Lemke D., Klaas U., Abolins J., et al., 1996, A&A 315, L64
Kessler M.F., Steinz J.A., Anderegg M.E., et al., 1996, A&A 315, L27
Klaas U., Laureijs R.J., Radovich M., Schulz B., 1998, Report on the ISOPHOT Calibration Accuracies, ISO Science Op. Center Report (SAI/98-092/Dc)
Komossa S., Greiner J., 1998, In: Poutanen J., Svensson R. (eds.) Proc. of High Energy Processes in Accreting Black Holes. Sweden, June 29 - July 4, 1998
Mas-Hesse J.M., Rodríguez-Pascual P.M., De Cordoba L.S.F., Mirabel F., 1994, ApJS 92, 599
Mas-Hesse J.M., Rodríguez-Pascual P.M., De Cordoba L.S.F., et al., 1995, A&A 298, 22
Mathis J.S., Rumpl W., Nordsieck K.H., 1977, ApJ 217, 425
Miller P., Rawlings S., Saunders R., Eales S., 1992, MNRAS 254, 93
Moran E.C., Halpern J.P., Helfand D.J., 1996, ApJS 106, 341
Mulchaey J.S., Koratkar A., Ward M.J., et al., 1994, ApJ 436, 586
Osterbrock D.E., Pogge R.W., 1985, ApJ 287, 166
Otani C., Kii T., Miya K., 1996, In: Zimmermann H. U., Trümper J., Yorke H. (eds.) Proc. Röntgenstrahlung from the Universe. MPE Report 263, 491
Pounds K.A., Done C., Osborne J., 1995, MNRAS 277, L5
Rodríguez-Pascual P.M., Mas-Hesse J.M., Santos-Lleó M., 1997, A&A 327, 72
Taylor J.R., 1982, An Introduction to Error Analysis. The Study of Uncertainties in Physical Measurements. University Science Books
Ulvestad J.S., Antonucci R.R.J., Goodrich R.W., 1995, AJ 109, 81
Véron-Cetty M.-P., Véron P., 1998, A Catalogue of Quasars and Active Nuclei. 8th Edition, European Southern Observatory Scientific Report No. 18 - June, 1998
Ward M.J., Geballe T., Smith M., Wade R., Williams P., 1987, ApJ 316, 138
Whittet D.C.B., 1992, Dust in the Galactic Environment. Institute of Physics Publishing, Bristol
Wisotzki L., Bade N., 1997, A&A 320, 395